Title

Modeling Climate Change Impacts on an Arctic Polygonal Tundra: 1. Rates of Permafrost Thaw Depend on Changes in Vegetation and Drainage

Journal

Journal of Geophysical Research Biogeosciences, 124(5)

ISSN

2169-8953

Authors

Grant, RF
Mekonnen, ZA
Riley, WJ

Publication Date

2019-05-01

DOI

10.1029/2018jg004644

Peer reviewed

Modeling Climate Change Impacts on an Arctic Polygonal Tundra: 1. Rates of Permafrost Thaw Depend on Changes in Vegetation and Drainage

R. F. Grant[1], Z. A. Mekonnen[2], and W. J. Riley[2]

[1] Department of Renewable Resources, University of Alberta, Edmonton, AB, Canada, [2] Earth Science Division, Lawrence Berkeley National Laboratory, Berkeley, CA, USA

Correspondence to: R. F. Grant, rgrant@ualberta.ca

Abstract

Model projections of permafrost thaw during the next century diverge widely. Here we used *ecosys* to examine how climate change will affect permafrost thaw in a polygonal tundra at Barrow AK. The model was tested against diurnal and seasonal variation in energy exchange, soil heat flux, soil temperature (T_s), and active layer depth (ALD) measured during 2014 and 2015, and interannual variation in ALD measured from 1991 to 2015. During RCP 8.5 climate change from 2015 to 2085, increases in T_a and precipitation (P) to 6.2 °C and 27% above current values, and in atmospheric CO_2 concentrations (C_a) to763 μmol mol^{-1}, altered energy exchange by increasing leaf area index of dominant sedge relative to that of moss. Increased C_a and sedge leaf area index imposed greater stomatal control of transpiration and reduced soil heat fluxes, slowing soil warming, limiting increases in evapotranspiration, and thereby causing gradual soil wetting. Consequently, increases in surface T_s and ALD of 2.4–4.7 °C and 21–24 cm above current values were modeled after 70 years. ALD increase was slowed if model boundary conditions were altered to improve landscape drainage. These rates were smaller than those of earlier modeling studies, some of which did not account for changes in vegetation, but are closer to those derived from current studies of warming impacts in the region. Therefore, accounting for climate change effects on vegetation density and composition, and consequent effects on surface energy budgets, will cause slower increases in T_s and ALD to be modeled during climate change simulations.

1 Introduction

There is currently much uncertainty about whether terrestrial landscapes in permafrost regions will become wetter or drier as climate change progresses (Schuur et al., 2015). Changes in Arctic soil water contents (θ) will be determined by changes in several interacting processes, including precipitation (P) versus evapotranspiration (ET), surface and subsurface hydrology (e.g., topographic effects on water transport, and permafrost effects on drainage), and soil warming.

Changes in θ may be determined by surface hydrology partly through changes in P versus ET. P in Arctic regions is generally expected to increase with climate change (Bintanja & Selten, 2014). However, ET in permafrost-

affected wetlands may be subject to various constraints that limit their response to warming, including increased ground heat flux (G) versus latent heat flux (LE) and increased moss surface resistance under high vapor pressure deficits (D; Liljedahl et al., 2011). These controls may therefore favor wetting in poorly drained landscapes.

Changes in θ may also be determined by surface hydrology partly through topographic effects on snow and water movement. Lower landscape features (e.g., troughs, low centers) retain deeper snowpacks and more near-surface soil water than do higher features (e.g., rims, high centers), and so may wet more as climate change progresses. Wetter soil has greater thermal conductivity and therefore ALD which may consequently increase with further soil wetting under climate change (Grant, Mekonnen, Riley, Wainwright, et al., 2017).

Changes in θ may also be determined by subsurface hydrology through changes in drainage caused by increasing active layer depths (ALD). Leffler et al. (2016) observed that artificial warming of an upland tussock tundra caused declines in θ from increased drainage with greater ALD. Some modeling studies have indicated that drainage of permafrost meltwater may cause upland Arctic landscapes with greater ALD to become drier (Avis et al., 2011). Lawrence et al. (2015) projected large-scale permafrost thaw and consequent soil drying due to increased drainage under an RCP 8.5 greenhouse gas emissions scenario. However, if drainage of permafrost meltwater is inhibited, poorly drained landscapes with smaller ALD may become wetter with increased P (Avis et al., 2011).

Changes in θ will also be affected by changes in soil temperatures (T_s) and ALD from changes in ground exposure to radiation caused by changes in vegetation density and composition. Current climate warming has been shown to increase density and alter composition of tundra vegetation (e.g., Elmendorf et al., 2012), and increased vegetation density has been shown to slow increases in T_s and ALD with warming (D. A. Walker et al., 2003). However, vegetation effects on ALD and consequently on soil wetting and warming during climate change remain largely unexamined.

The complexities of hydrological and vegetative effects on ALD cause uncertainties in ALD projections with climate change. In a model calibration, Harp et al. (2016) simulated an increase in ALD of a peatland at the Barrow Experimental Observatory (BEO) from approximately 0.3 m in 2006 to nearly 0.9 m in 2100 under the RCP8.5 emission scenario in which vegetative processes were not represented. In a pan-Arctic study, Koven et al. (2011) modeled increases in ALD from 0.4 m in 1990–2000 to greater than 1 m in 2090–2100 in coastal northern Alaska where the BEO is located. However, the effects of surface topography and of changes in hydrology and vegetation on ALD during climate change need to be more explicitly represented in models used in these projections.

Changes in T_s, θ, and ALD will strongly affect changes in CO_2 and CH_4 exchange in Arctic landscapes as climate change progresses. Soil warming is expected to hasten decomposition of permafrost C and thereby release of CO_2 and CH_4 to the atmosphere which would hasten climate change (Schuur et al., 2015). It is therefore important that changes in T_s, θ, and ALD be accurately projected under specified climate change scenarios. In an earlier modeling study (Grant, Mekonnen, Riley, Wainwright, et al., 2017) we modeled topographic effects on changes in θ and ALD at BEO as affected by interannual variation in air temperature (T_a) and P under current climate (1981–2015). In a companion study (Grant, Mekonnen, Riley, Arora, et al., 2017) we modeled the effects of these changes in θ and ALD on CO_2 and CH_4 exchange at BEO. In both studies, model results were tested against field data recorded at BEO in the Next Generation Ecosystem Experiment-Arctic.

Building on these earlier studies, in this paper we present model projections from 2016 to 2085 under a RCP8.5 emission scenario of changes in T_s, θ, and ALD (this paper), and thereby in CO_2 and CH_4 exchanges (companion paper) in an Arctic polygonal landscape at BEO. We hypothesize that effects on T_s, θ, and ALD will be determined by evolving interactions among T_a, P, hydrology, and vegetation as climate change progresses:

1. Increasing T_a will reduce effluxes of sensible heat from canopy and ground surfaces to the atmosphere, causing them to warm relative to current climate. However, canopy warming will increase vegetative growth and leaf area index (LAI) which will reduce net radiation (R_n) at the ground surface, slowing soil warming.
2. P will increase more than ET, which will be constrained by increasing surface resistances caused by changes in composition and density of vegetation, causing soil wetting in poorly drained polygonal tundra.
3. Soil warming in (1) and wetting in (2) will cause increases in ALD that will differ between higher features with better drainage and lower features with poorer drainage within polygonal tundra landscapes.
4. Soil wetting in (2) and increases in ALD in (3) will be reduced if changes in hydrology external to the polygonal tundra increase drainage of meltwater from permafrost thawing as climate change progresses.

2 Model Description

E*cosys* is an hourly time step model with multiple canopy and soil layers that provide a framework for multispecific plant and microbial populations to acquire, transform, and exchange resources (energy, water, C, N, and P). The model is constructed from algorithms representing basic physical, chemical, and biological processes that determine process rates in plant and microbial populations interacting within complex biomes. These algorithms interact to simulate complex ecosystem behavior across a wide range of spatial scales from square meter to continental. The model is designed to represent

terrestrial ecosystems under a range of natural and anthropogenic disturbances and environmental changes at patch (spatially homogenous one-dimensional) and landscape (spatially variable two- or three-dimensional) scales.

Key model equations and their parameterizations used to test the hypotheses in this study are described in supplements S1 through S8 in the supporting information to this article and summarized in Table 1. These equations are cited with regard to key model processes in section 5 below; reference to these equations in the supporting information is intended to provide insight into model behavior, but is not required to understand model results. Of particular relevance to this study are equations in S4: *Soil Water, Heat, Gas and Solute Fluxes* that represent physical processes governing the exchange of heat, water, and gases between ecosystem surfaces through first order closures of energy balances at canopy, snowpack, litter, and soil surfaces [B1, D11], fully coupled with convective-diffusive transport of heat, water, snow, gases, and solutes according to thermal [D12], hydraulic [D9], gaseous [D17], and aqueous [D20] conductivties in vertical and lateral directions through snowpacks, surface litter, and soil in topographically variable landscapes. These coupled processes drive transformations of heat and water through freezing and thawing in snowpacks, surface litter, and soil by solving the general heat flux equation [D13] required to examine hypotheses (1), (3), and (4) above. Algorithms in S2: *Soil-Plant Water Relations* represent physical processes driving soil-plant-atmosphere water transfer using coupled algorithms for hydraulically driven root water uptake [B6] with energy-driven canopy transpiration [B1]. These algorithms are fully coupled with those for plant CO_2 fixation and growth by diverse plant functional types (PFT) competing for common resources of irradiance and nutrients in S3: *Gross Primary Productivity, Autotrophic Respiration, Growth and Litterfall* through canopy water potential and stomatal conductance [C4] required to test hypothesis (2) and its implications for hypotheses (3) and (4) above. CO_2 fixation and nutrient uptake by each PFT are driven by vertical profiles of leaf area and root length modeled prognostically from biometric conversions of nonstructural C, N, and P assimilated by leaves and roots within common canopy and soil layers [C21a–c]. All parameters in these algorithms are unchanged from those the earlier studies at BEO (Grant, Mekonnen, Riley, Wainwright, et al., 2017; Grant, Mekonnen, Riley, Arora, et al., 2017).

Table 1
List of Supplements in the Supporting Information

Supplement	Title	Equations
S1	Microbial C, N and P Transformations	[A1]–[A39]
S2	Soil-Plant Water Relations	[B1]–[B14]
S3	Gross Primary Productivity, Autotrophic Respiration, Growth and Litterfall	[C1]–[C53]
S4	Soil Water, Heat, Gas and Solute Fluxes	[D1]–[D21]
S5	Solute Transformations	[E1]–[E57]
S6	Symbiotic N_2 Fixation	[F1]–[F26]
S7	CH_4 Production and Consumption	[G1]–[G27]
S8	Inorganic N Transformations	[H1]–[H21]

3 Site Description

The BEO is located ~6 km east of Barrow, AK (71.3°N, 156.5°W), at the northern tip of Alaska's Arctic coastal plain. Barrow has a maritime climate characterized by long, dry winters and short, moist, cool summers, with a mean annual air temperature (MAT_a) of −12 °C and mean annual P of 106 mm. Continuous ice-rich permafrost extends to >400 m depth, overlain by a shallow active layer whose depth varies spatially and interannually from approximately 20 to 60 cm. The BEO is more fully described in Dafflon et al. (2016, 2017), Vaughn et al. (2016), and Wainwright et al. (2015).

4 Model Experiment

4.1 Model Spinup

4.1.1 Model Initialization

We defined the *ecosys* computational domains from the polygon classification scheme of Wainwright et al. (2015), in which polygons of 5–20 m at BEO were resolved into different types based on surface elevations. The low-centered polygonal (LCP) landform was represented as a center 6 m in width and length, surrounded by a rim 1 m in width and 0.2 m in height above the center, which was surrounded in turn by a trough 1 m in width and 0.2 m in depth below the rim. Each feature was represented by a number of interconnected grid cells (Figure 1a). The trough and the center were connected through a 1 m breach in the rim, based on the observation of Dafflon et al. (2017) that LCP ridges are variable in height. The flat-centered polygonal (FCP) landform was represented by features with the same dimensions, but the center was level with the rim (Figure 1b). The landform surfaces were thus 36% centers, 28% rims, and 36% troughs, similar to those derived from a high-resolution digital elevation model by Kumar et al. (2016). Other landforms such as high-centered polygons were not represented at this stage of model testing, based on the findings of Wainwright et al. (2015) that 47% of the BEO landscape is occupied by FCPs, and most of the remainder by LCPs.

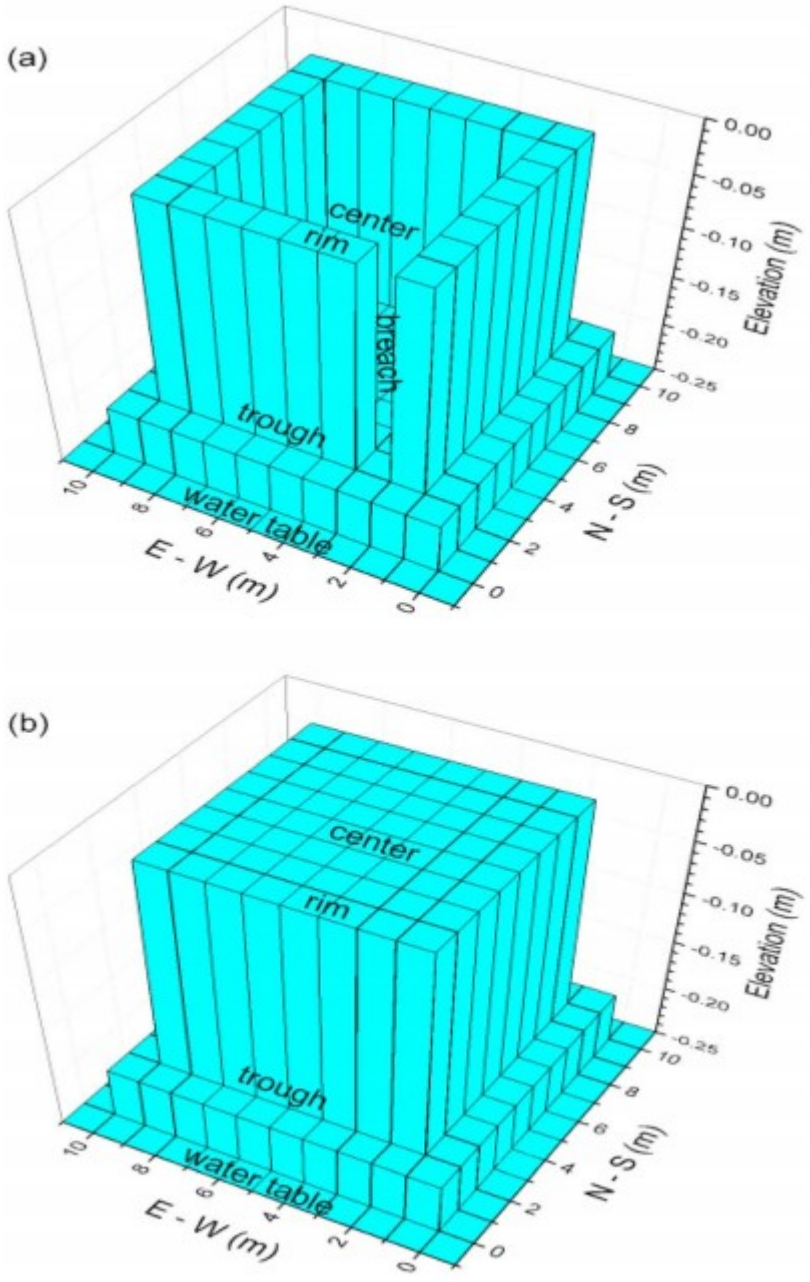

Figure 1. Representation in *ecosys* of microtopography in (a) low-centered and (b) flat-centered polygon. Elevations are expressed with respect to the rim surface.

Barrow soil types are generally classified as Gelisols, with an organic-rich soil layer underlain by a cryoturbated mineral soil (silty clay to silty loam-textured) layer and a frozen organic-rich mineral layer. Soil profiles representing the key properties of the centers, rims, and troughs used in *ecosys* (Table 2 of Grant, Mekonnen, Riley, Wainwright, et al., 2017) were assigned to each grid cell within each feature (Figure 1). Measurements of

these properties indicated greater variation within than among features with no consistent topographic effects on soil horizonation (Kumar et al., 2016). Therefore, soil properties in each feature were assumed to be the same at any depth relative to its surface so that differences in modeled hydrological and thermal conditions among features could be attributed solely to microtopographic effects.

4.1.2 Model Boundary Conditions

Surface boundary conditions were set to allow overland flow of excess surface water from troughs at the northern and southern boundaries of the modeled polygons. Snow movement across external surface boundaries was not modeled. Overland movement of water and snow among features within each landform was modeled from higher to lower topographic positions. Subsurface boundary conditions were set to allow lateral discharge and recharge of water driven by elevation differences between water tables in the troughs and an external water table set to a depth of 0.025 m below and a distance of 2.5 m from the trough surfaces at the northern and southern boundaries of the modeled polygons [D10] (Figure 1; Grant, Mekonnen, Riley, Arora, et al., 2017). This placement of the external water table near the troughs was suggested by observations that troughs often serve as pathways for water movement through polygonal landscapes (Liljedahl et al., 2012; Woo & Guan, 2006). The water table depth (WTD) in each grid cell was that at which the difference between P and ET from the surface energy balance within each grid cell equilibrated with the difference between discharge to and recharge from adjacent grid cells [D7]. An upward geothermal flux of 57 mW/m^2 was maintained across the lower boundary (Sclater et al., 1980).

Each grid cell in the LCP and FCP was initialized with the same populations of sedge (200 plants per square meter) and moss (10^4 plants per square meter) and soil porosity fully occupied by ice on 1 January in the model year 1980. Both model polygons were run from 1980 to 2015 using gap-filled ½-hourly meteorological data (shortwave and longwave radiation, air temperature, relative humidity, windspeed, and P) from 1 January 1981 to 15 June 2013 derived by Xu and Yuan (2016) from the Barrow, AK, station of NOAA/Earth System Laboratory, Global Monitoring Division (http://www.esrl.noaa.gov/gmd/obop/brw/), and NOAA's National Climate Data Center, and from 16 June 2013 to 31 December 2015 using 1-hourly meteorological data recorded at BEO by Hinzman et al. (2016). Atmospheric NH_3 concentration driving dry N deposition [D15] was set to 0.5 nmol mol^{-1} (Wentworth et al., 2016) and P NH_4^+ and NO_3^- concentrations driving wet deposition were both set to 0.1 g N m^{-3} based on N deposition maps from the National Atmospheric Deposition Program. Results from these runs were presented in Grant, Mekonnen, Riley, Wainwright, et al. (2017) and Grant, Mekonnen, Riley, Arora, et al. (2017).

4.2 Model Runs

The model spinup described in section 4.1 was extended through two additional 35-year cycles from model dates 1 January 2016 to 31 December 2085. These extended runs were conducted under the following meteorological boundary conditions to attribute climate change effects on ALD to increases in T_a, C_a, P, and drainage in polygonal tundra:

1. *Baseline*. Meteorological data in both cycles remained unchanged from those recorded from 1981 to 2015 (section 4.1) and atmospheric CO_2 concentration (C_a) was maintained at its 2015 value to ascertain that model results remained stable for the 70-year duration of the run. Stability would be achieved if results during the second 35-year cycle remained the same as those during the first.
2. $+T_a$. Values of T_a in (1) were incremented hourly by the increases in maximum and minimum T_a derived under a RCP 8.5 emission scenario downscaled and averaged across 15 CMIP5 models for the grid cell in which BEO is located (Table 2). Relative humidity in (1) was assumed to remain constant, so that atmospheric vapor pressures (e_a) rose with T_a.
3. $+T_a + C_a$. Meteorological data in (2) were used with C_a incremented hourly by the increases expected under a RCP 8.5 emission scenario (Table 2).
4. $+T_a + C_a + P$ (*full climate change*). Meteorological data and C_a in (3) were incremented hourly by the increases in P derived under a RCP 8.5 emission scenario (Table 2).
5. $+T_a + C_a + P + 1$. (4) was rerun with the depth of the external water table (section 4.1) lowered by 1 cm after every 10 years to project climate change effects on soil wetting and ALD under gradual increases in drainage of polygonal tundra.
6. $+T_a + C_a + P + 2$. (4) was rerun with the depth of the external water table (section 4.1) lowered by 2 cm after every 10 years to project climate change effects on soil wetting and ALD under more rapid increases in drainage of polygonal tundra.

Table 2

Seasonal Increases in Average Maximum and Minimum Temperatures and Increases in Precipitation and Atmospheric CO_2 Concentration (C_a) Relative to Current Values From 1981–2010 to 2071–2100 Under a RCP 8.5 Emission Scenario Downscaled and Averaged Across 15 CMIP5 Models for the Grid Cell in Which Barrow Experimental Observatory is Located

	Winter (DJF)	Spring (MAM)	Summer (JJA)	Autumn (SON)
Max. Temp. (°C)	10.97	7.08	4.53	7.25
Min. Temp. (°C)	12.80	8.28	4.84	8.30
Precipitation (−)	1.34	1.52	1.28	1.34
C_a (−)	2.37	2.37	2.37	2.37

Note. DJF = December-January-February; MAM = March-April-May; JJA = June-July-August; SON = September-October-November.

In all runs with $+T_a$, acclimation was modeled by gradually shifting the Arrhenius functions used to simulate the temperature sensitivities of all biological processes contributing to GPP [C10a–e], R_a [C22a,b], and R_h [A6, A19] to the right by 0.3 °C for each 1 °C of warming as described in an earlier modeling study (Figure 1 in Grant, 2015).

4.3 Model Tests

4.3.1 Artificial Soil Heating Experiment

The sensitivity of modeled θ to soil warming was investigated by simulating an artificial soil heating experiment conducted at BEO in which a 1.4 amp heating rod was installed vertically to a depth of 50 cm within a 30-cm diameter PVC collar installed to a depth of 35 cm in a center of a high-centered polygon. Power through the heating rod was adjusted to maintain T_s averaged from 10 to 35 cm depth at 4 °C above those in a control plot from June to October in 2015. This experiment was simulated by running *ecosys* during 2015 of the FCP spinup run with energy added each hour to all soil layers in the upper 50 cm of a center grid cell to maintain a 4 °C increase in T_s from 1 June to 31 October relative to those of the same grid cell in a control run (Figure 1; Table 2 in Grant, Mekonnen, Riley, Wainwright, et al., 2017). Lateral movements of heat and water between the heated and adjacent grid cells were disabled to the depth of the PVC collars (35 cm).

4.3.2 Next Generation Ecosystem Experiment-Arctic

Results from the baseline run for energy fluxes and T_s in 2084 and 2085 modeled under 2014 and 2015 weather were tested with energy fluxes and T_s measured at the BEO by Dengel et al. (2017) and Romanovsky and Cable (2017). Testing was conducted by evaluating intercepts (a), slopes (b), correlations (R^2), and root-mean-square for differences (RMSD) from regressions of measured on modeled values, representing variation in measured values not explained by the model. A successful test was indicated by values of a near zero, b near one ($1.1 > b > 0.9$), R^2 greater than that at $p = 0.001$, and RMSD similar to variation in measured values caused by measurement uncertainty, indicating limited opportunity for improving agreement between modeled and measured values. Values of ALD modeled in rims and troughs during 2084 of the baseline run under 2014 weather were compared with values measured in 2014 by Peterson (2017).

5 Results

5.1 Effects of Artificial Soil Heating on Soil Water Content

Values of T_s modeled at 10 cm in the unheated control grid cell at the FCP center were highly correlated with those measured in centers of high-centered polygons at BEO during 2015 (Table 3), although measurements were taken at a slightly higher elevation. Modeled T_s rose above 0 °C earlier in spring than did measured T_s, and modeled θ rose above frozen values earlier than did measured θ (Figures 2b and 2c), indicating earlier spring

thawing in the model caused by a slight underestimation of snow accumulation and hence earlier snowmelt modeled in FCP centers (Figure 7 in Grant, Mekonnen, Riley, Wainwright, et al., 2017). Measurement of model inputs for P as snowfall is a key source of uncertainty in modeling Arctic hydrology. Declines in T_s and θ modeled during autumn were similar to those measured, indicating that autumn freezing was accurately modeled. Both measured and modeled θ remained below saturated values (0.73 in Grant, Mekonnen, Riley, Wainwright, et al., 2017) due to the 0.225 m elevation of the FCP center grid cell above the water table (Figure 1b).

Table 3

Statistics From Regressions of Hourly Soil Temperatures Measured at 10 cm in High-Centered Polygon Centers by Romanovsky and Cable (2017) on Those Modeled at 10 cm in a Flat-Centered Polygon Center Grid Cell at Barrow Experimental Observatory From 1 June to 31 October in 2015

Year	a[a]	b[a]	R^2	RMSD[b]	n
2015	0.19	0.90	0.92[c]	0.58	3,595

Note. RMSD = root-mean-square for difference.
[a]$Y = a + bX$ from regression of measured Y on simulated X. [b]RMSD from regression of measured Y on simulated X. [c]Significant at $p \ll 0.001$.

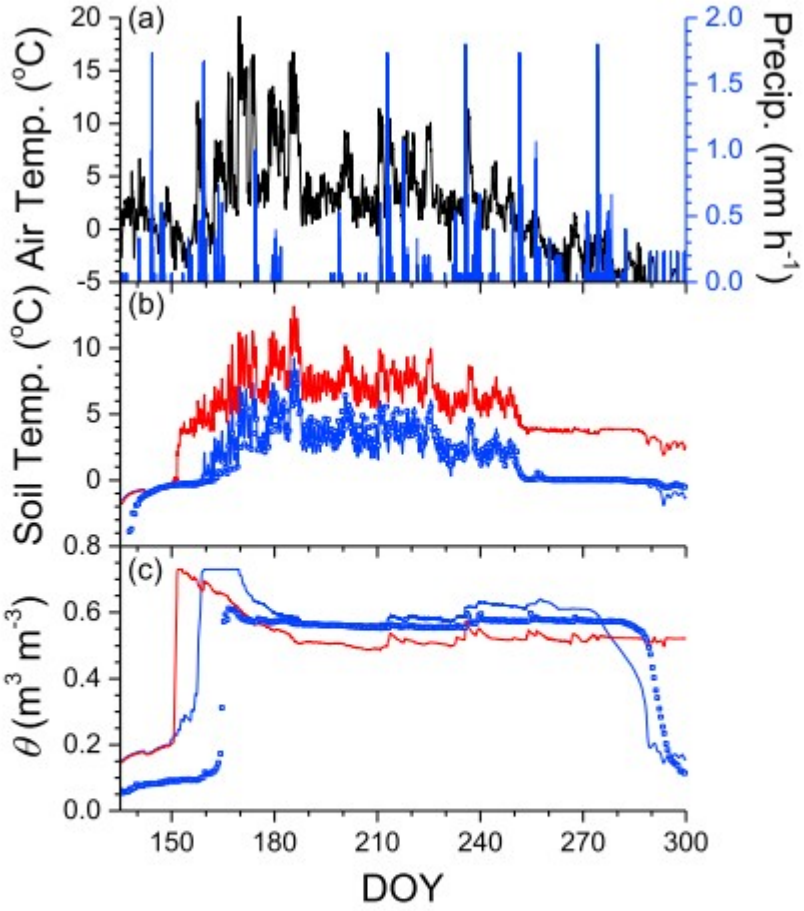

Figure 2. (a) Air temperature and precipitation, and (b) soil temperatures and (c) water contents (θ) modeled (lines) and measured (symbols) at 10 cm depth in control (blue) and artificially warmed (red) flat-centered polygon centers during 2015. Measured data from high-centered polygon centers by Romanovsky and Cable (2017). DOY = day of year.

Energy added to soil layers in the upper 50 cm of the warmed grid cell maintained a stable increase in T_s of 4 °C from that modeled in the control grid cell (Figure 2b). This increase drove soil drying which caused θ to decline below that modeled in the control grid cell (Figure 2c). This drying was modeled because the added energy reduced *G* influxes and increased *H* and *LE* effluxes (e.g., during early July in Figure 3). These changes in energy balance caused *ET* modeled from 1 June to 31 October in the warmed grid cell to be 53% greater than that in the control. Plant transpiration modeled during this period was only slightly increased by warming, so that almost all soil drying (Figure 2c) was attributed to increased evaporation.

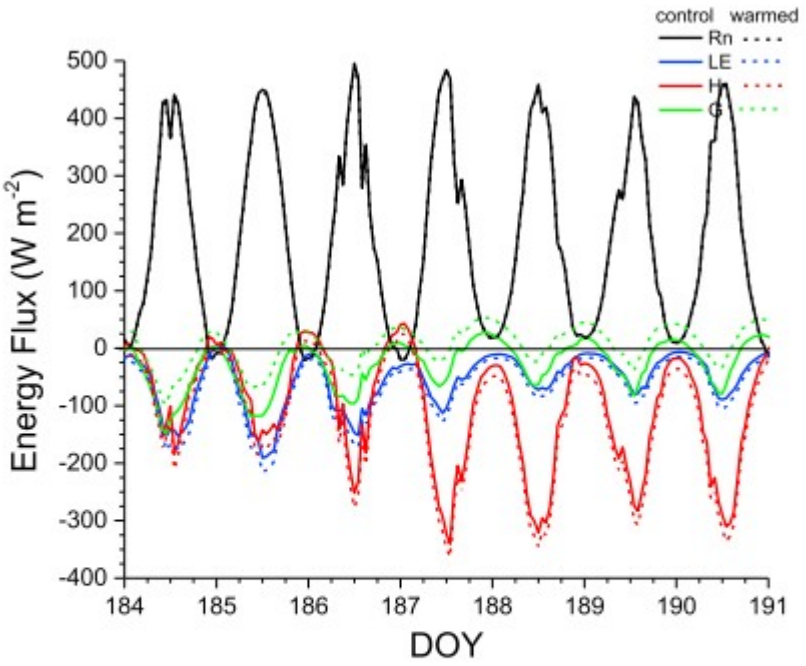

Figure 3. R_n, LE, H, and G fluxes modeled over control and warmed (+4 °C) soil during early July 2015 at Barrow Experimental Observatory. Positive values of H, R_n, and LE represent influxes, and negative values effluxes. Positive values of G represent heat loss, and negative values heat gain. R_n = net radiation; LE = latent; H = sensible; G = soil; DOY = day of year.

5.2 Model Results From Baseline Run

5.2.1 Energy Exchange and Soil Temperature

The baseline run from 2016 to 2085 consisted of two repeating 35-year weather sequences (2016–2050 and 2051–2085) of 1981–2015 weather following spinup from 1981 to 2015 (section 4.2). During the final year of the second sequence in 2085 with 2015 weather, modeled energy fluxes were spatially aggregated over all grid cells in the LCP and FCP and compared with EC measurements during a transition from warm to cool weather under stable radiation in early July (Figure 4a). Higher T_a (day of year 185–186 in Figure 4a) caused increases in LE and G, and commensurate decreases in H relative to those under lower T_a (day of year 188–191; Figure 4b).

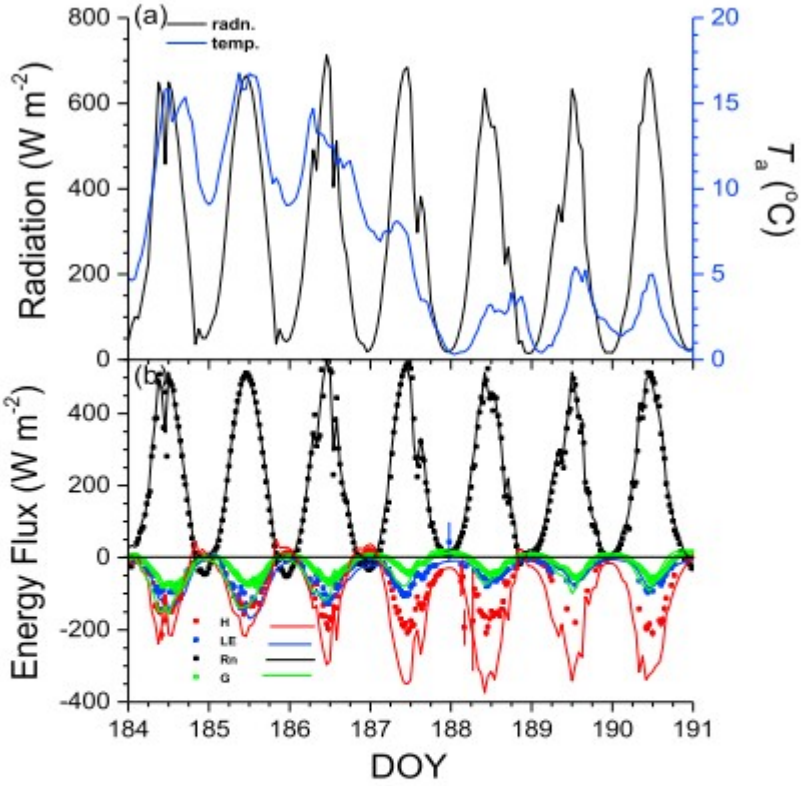

Figure 4. (a) Radiation and air temperature; (b) R_n, *LE*, *H*, and *G* fluxes measured (symbols) and modeled (lines) during a transition from warm to cool weather during early July 2015 (measured) and with 2015 weather during early July 2085 of the baseline run. Positive values of *H*, R_n, and *LE* represent influxes, and negative values effluxes. Positive values of *G* represent heat loss, and negative values heat gain. Measured EC fluxes from Dengel et al. (2017). R_n = net radiation; *LE* = latent; *H* = sensible; *G* = soil; DOY = day of year.

Spatially aggregated energy fluxes modeled from all grid cells in the LCP and FCP during 2084 and 2085 of the baseline run with 2014 and 2015 weather were regressed on EC measurements during 2014 and 2015. These regressions indicated that modeled *LE* was slightly underestimated in 2014 ($b > 1$) and overestimated in 2015 ($b < 1$; Table 4). However, modeled *H* and *G* were overestimated in both years ($b < 1$; e.g., Figure 4b). To some extent, model overestimates of aerodynamic fluxes *H* and *LE* were expected due to incomplete energy balance closure in EC measurements, while comparisons of modeled versus measured *G* may be affected by the measurement depth which can cause measured *G* to be underestimated (Gentine et al., 2012). Values of RMSD for variation in measured values not explained by the model were in most cases about twice those of root-mean-square error for variation in measured values caused by measurement uncertainty, indicating limited opportunity to improve agreement between modeled and measured values.

Table 4

Statistics From Regressions of Hourly Averaged R_n, LE, H, and G Heat Fluxes Measured by Dengel et al. (2017) on Those Modeled Over Combined Low-Centered Polygon and Flat-Centered Polygon Landforms at Barrow Experimental Observatory During Growing Seasons of 2014 and 2015

Flux	a[a]	b[a]	R^2	RMSD[b]	RMSE[c]	n
	W/m^2			W/m^2	W/m^2	
2014						
R_n	−9.5	0.91	0.93[d]	28	nd	4,076
LE	0.2	1.15	0.71[d]	17	13	1,190
H	−2.1	0.75	0.88[d]	22	8	1,714
G	−1.5	0.30	0.57[d]	11	5	3,390
2015						
R_n	−9.6	1.05	0.95[d]	29	nd	3,936
LE	−3.0	0.85	0.77[d]	19	9	813
H	−8.6	0.63	0.85[d]	23	16	1,027
G	0.7	0.42	0.72[d]	11	5	3,936

Note. R_n = net radiation; *LE* = latent; *H* = sensible; *G* = soil; RMSD = root-mean-square for difference; RMSE = root-mean-square error.

[a]$Y = a + bX$ from regression of measured Y on simulated X. [b]RMSD from regression of measured Y on simulated X. [c]RMSE estimated from EC measurements by Billesbach (2011). [d]Significant at $p \ll 0.001$.

5.2.2 Active Layer Depth

The seasonal development of the active layer modeled in the baseline run during 2084 with 2014 weather was compared with that measured during 2014 in centers of the LCP and FCP (Figure 5). In the model, *G* [D11] (e.g., Figure 4b) drove vertical and horizontal soil heat transfers [D12] that in turn drove soil freezing and thawing [D13], and hence active layer development. Modeled thawing allowed ALD to follow values measured in centers of LCP (Figure 5a) and FCP (Figure 5c). Both modeled and measured ALD reached greater maximum values in the lower LCP center (39 and 39 cm) than in the higher FCP center (35 and 34 cm) because wetter soils in lower features had greater thermal conductivity [D12d] and hence thawed more rapidly (Grant, Mekonnen, Riley, Wainwright, et al., 2017). Differences in ALD modeled with surface elevation were smaller in 2014 than in earlier years because of greater antecedent *P* and hence greater θ in higher features.

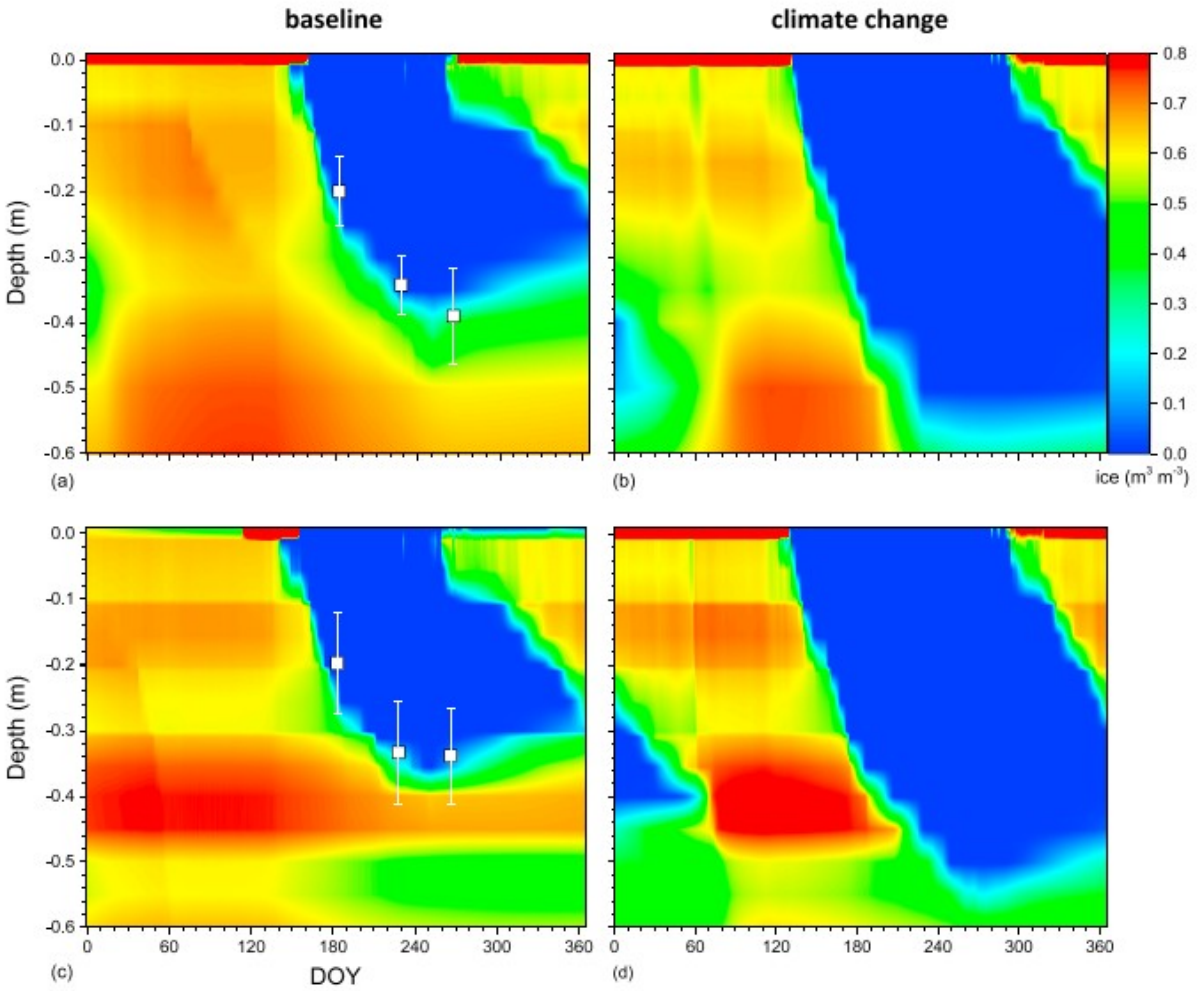

Figure 5. Ice contents of surface litter and soil profiles modeled during 2084 in centers of the (a and b) low-centered polygon and (c and d) flat-centered polygon in the baseline (a and c) and climate change (b and d) runs. Active layers are indicated by ice-free zones in dark blue. Symbols represent measurements of active layer depth in 2014 by Peterson (2017). DOY = day of year.

Values of ALD modeled during the second sequence of the baseline run (2051–2085) closely followed those during the first (2016–2050) for all features of the LCP and FCP (b = 0.98–1.00, R^2 = 0.96–0.99; Figures 6b and 6c), indicating that hydrology in the model remained in equilibrium for the 70 year duration of the run following the initial spinup from 1981 to 2015. ALD modeled in lower landform features (troughs, LCP centers) maintained close agreement with ALD measured in the Circumpolar Active Layer Monitoring program (https://www2.gwu.edu/~calm/data/north.html accessed 27 April 2017) and in site studies. ALD modeled in higher features (rims, FCP centers) were shallower, but similar to or greater than minimum ALDs of 0.17 m averaged from 1995 to 2009 in polygonal tundra at Barrow by Shiklomanov et al. (2010). During both sequences, modeled and measured ALD increased with MAT_a and annual P, as described in an earlier modeling study at BEO (Grant, Mekonnen, Riley, Wainwright, et al., 2017). Some of the measured

increase may have been offset by surface subsidence which is not yet simulated in *ecosys*. However, subsidence would not directly affect the soil mass within the active layer, which would increase with deepening of the permafrost surface.

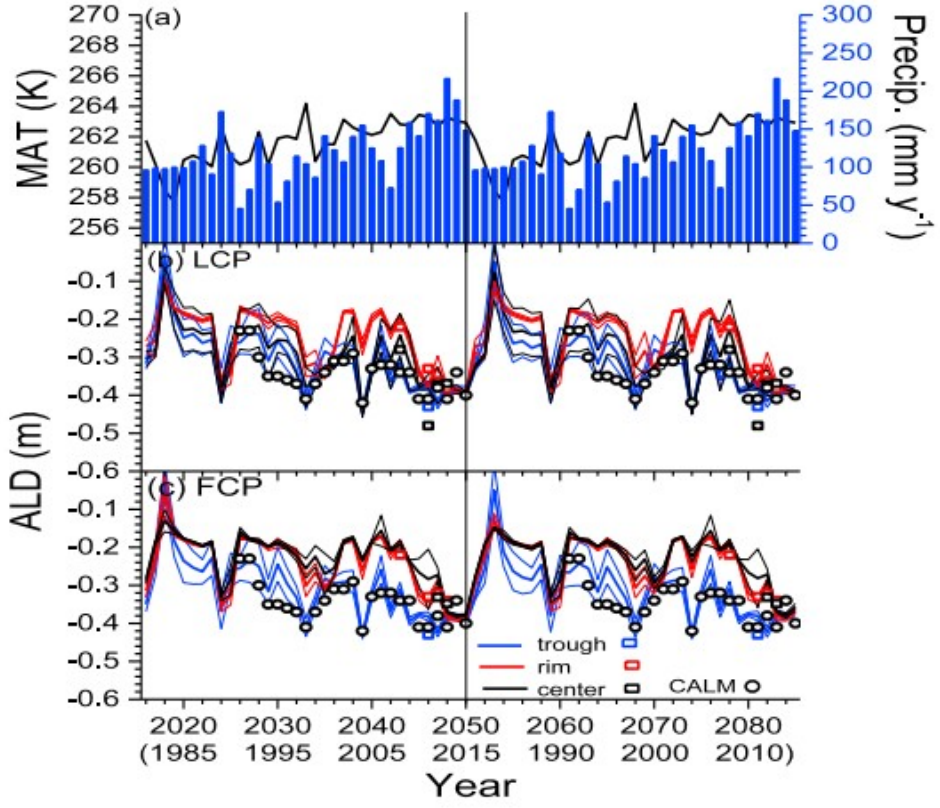

Figure 6. (a) Mean annual temperature (line) and annual precipitation (bars) at Barrow, AK, from 1981 to 2015 used in the baseline run from 2016 to 2050 and from 2051 to 2085, and ALD modeled (lines) on 31 August in troughs, rims, and centers of the (b) LCP and (c) FCP and measured in late August 1991–2009 at the CALM site in Barrow Experimental Observatory (open circles), late August 2008 by Zona et al. (2011), and in early September 2012–2013 by Wood et al. (2015; open squares). Thinner lines indicate standard deviation of values modeled for all grid cells in each feature. Meteorological data from Xu and Yuan (2016) and Hinzman et al. (2016). ALD = active layer depth; MAT = mean annual temperature; LCP = low-centered polygon; FCP = flat-centered polygon; CALM = Circumpolar Active Layer Monitoring.

5.3 Effects of Climate Change on Ecosystem Hydrology

5.3.1 Energy Exchange

The effects of climate change on ecosystem energy exchange and temperatures were examined by comparing results during the transition from warm to cool weather in early July of 2085 in the baseline run with 2015 weather (Figure 4) with those during the same period after 70 years of $+T_a + C_a + P$ (Table 2 and Figure 7a). Fluxes of R_n, LE, H, and G modeled with $+T_a + C_a + P$ were all reduced slightly from those in the baseline run (Figure 7b) in spite of an increase in T_a of *ca*. 4 °C (Figure 7a). However, responses of energy fluxes to short-term changes in T_a modeled with $+T_a + C_a + P$ remained similar to those modeled in the baseline run, indicating that

changes in energy fluxes with T_a differed between short-term changes in weather and long-term changes in climate.

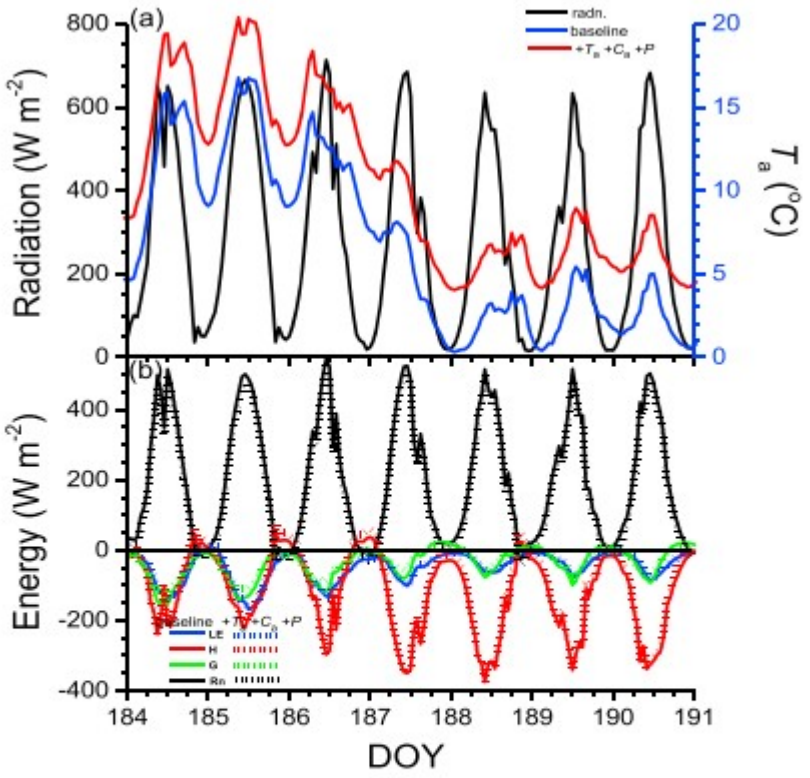

Figure 7. (a) Radiation and air temperature (T_a) from the baseline and $+T_a + C_a + P$ runs, (b) R_n, LE, H, and G heat fluxes modeled during a week in early July 2085 in the baseline and $+T_a + C_a + P$ runs. Positive values of H, R_n, and LE represent influxes, and negative values effluxes. Positive values of G represent heat loss, and negative values heat gain. R_n = net radiation; LE = latent; H = sensible; G = soil; DOY = day of year.

Reductions in energy fluxes modeled with $+T_a + C_a + P$ were caused by increases in density and changes in composition of vegetation. Sedge LAI in the model increased with climate change, particularly in higher features (LCP rims and FCP rims and centers in Table 5), as described in the accompanying paper (Grant et al., 2019). Because sedge in the model was taller than moss, greater sedge LAI caused increases in sedge R_n. However, these increases were offset by larger decreases in moss and ground R_n from increased shading by sedge (Figure 8a), so that total R_n declined slightly (Figure 7b). Increases in sedge R_n drove only small increases in sedge LE effluxes because sedge r_c rose with C_a [C5], and consequently drove larger increases in H effluxes (Figures 8b and 8c). However, these increases were offset by decreases in LE and H effluxes from moss and the ground surface, so that ecosystem LE and H also declined slightly (Figure 7b). Increases in sedge R_n, LE, and H caused increases in sedge canopy temperatures (T_c; Figure 8e) that were similar to those in T_a (Figure 7a). However, decreases in R_n at the

ground surface were only partially offset by decreases in *LE* effluxes (Figure 8b) and by increases in *H* influxes (advection; Figure 8c), causing smaller gains in *G* (Figure 8d) and hence smaller rises in T_s with T_a relative to those in the baseline run (Figure 8e). Therefore, increased shading caused T_s in the model to rise more slowly with $+T_a + C_a + P$ than did T_a.

Table 5
Leaf Area Indices (in m^2/m^{-2}) of Sedge and Moss Modeled in Troughs, Rims, and Centers During Early July 2085 in the Baseline and $+T_a + C_a + P$ Runs

	Trough		Rim		Center	
	Sedge	Moss	Sedge	Moss	Sedge	Moss
	Baseline					
LCP	0.53	1.42	0.48	1.23	0.55	1.43
FCP	0.53	1.52	0.50	1.36	0.48	1.26
	$+T_a + C_a + P$					
LCP	0.93	1.54	1.01	1.70	0.92	1.57
FCP	0.91	1.64	1.02	1.86	0.96	1.73

Note. LCP = low-centered polygon; FCP = flat-centered polygon.

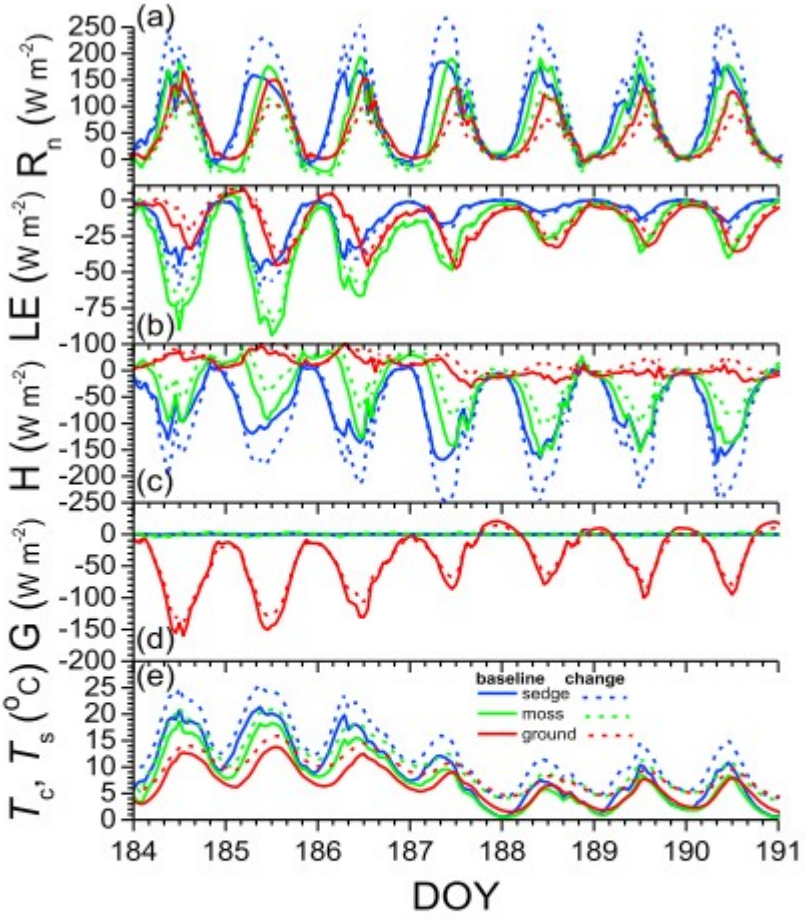

Figure 8. (a) R_n, (b) *LE*, (c) *H*, (d) *G*, and (e) canopy and soil surface temperatures T_c and T_s modeled in a low-centered polygon trough during a week in early July 2085 in the baseline (solid lines) and $+T_a + C_a + P$ (dotted lines) runs. In (a)–(c) positive values of R_n, *LE*, and *H* represent influxes, and negative values effluxes. In (d) positive values of *G* represent heat loss, and negative values heat gain. R_n = net radiation; *LE* = latent; *H* = sensible; *G* = soil; DOY = day of year.

5.3.2 Active Layer Depth

Gains in *G* modeled with increased *H* from advection at the ground surface during spring under $+T_a + C_a + P$ increased vertical and horizontal soil heat transfers [D12] that slowed freezing and hastened thawing [D13]. These increases extended the duration and depth of the ice-free soil zone (e.g., Figures 5b and 5d vs Figures 5a and 5c) and hence gradually increased ALD of all landform features (Figures 9b and 9c) from those in the baseline run (Figures 6b and 6c). However, these increases were greater in features with higher elevation than in those with lower, causing a gradual convergence of ALD among features as climate change progressed. Average rates of ALD increase with $+T_a + C_a + P$, calculated from spatially averaged differences with the baseline run for all features, were 3.1 and 3.4 cm per decade in the

LCP and FCP, respectively. In lower features, most of these increases were attributed to warmer soils from rising T_a (Figure 10a) but in higher features, increasing fractions of these increases were attributed to wetter soil from rising P, particularly in drier years, as climate change progressed (Figure 10b).

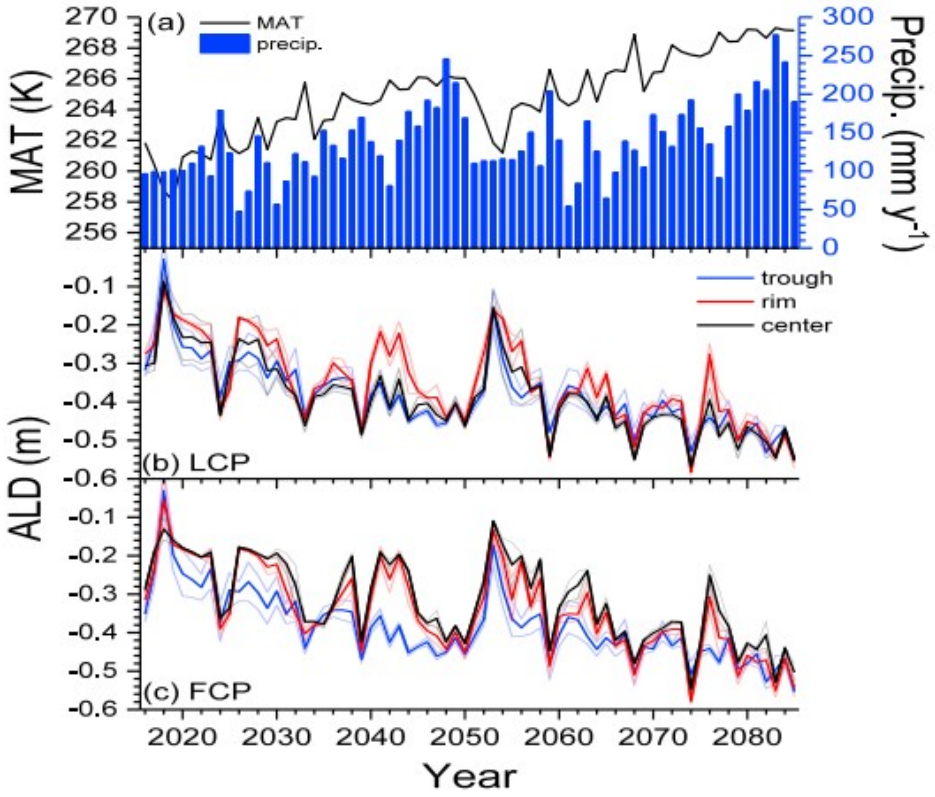

Figure 9. (a) MAT (line) and annual precipitation (bars) at Barrow, AK, with meteorological data from 1981 to 2015 incremented hourly from 2016 to 2085 with changes in T_a, C_a and precipitation ($+T_a + C_a + P$), and ALD modeled on 31 August in troughs, rims, and centers of the (b) LCP and (c) FCP. ALD = active layer depth; MAT = mean annual temperature; LCP = low-centered polygon; FCP = flat-centered polygon.

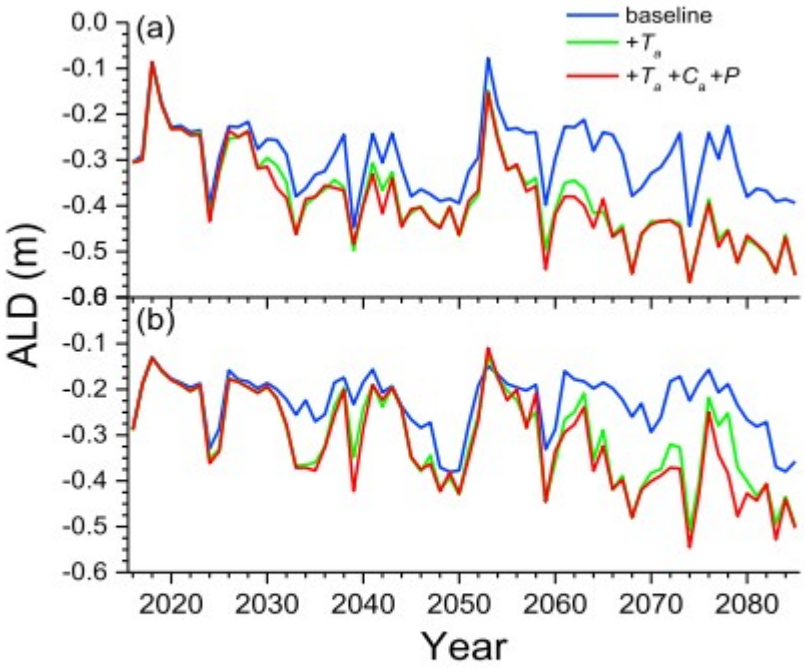

Figure 10. ALD modeled on 31 August in centers of the (a) low-centered polygon and (b) flat-centered polygon in the baseline run, and in climate change runs with increments of T_a ($+T_a$) and of T_a, C_a, and P ($+T_a + C_a + P$). ALD = active layer depth.

Drainage into permafrost was prevented by ice and bound water which occupied the entire soil porosity in the modeled permafrost zone (e.g., Figure 5), so that water tables were modeled within the active layer above the permafrost table of each feature. Constraints on ET modeled with $+T_a + C_a + P$ (Figure 7b and Figure 8b) caused these water tables to rise above those in the baseline run with increasing P as climate change progressed (Table 2). Thus, WTDs modeled in 2085 of both the baseline and the $+T_a + C_a + P$ runs increased with low P before mid-July (Figure 11a), but WTDs in the $+T_a + C_a + P$ run declined more rapidly from increased P thereafter (Figures 11b–11d). Consequent increases in θ of surface litter and surface soil raised thermal conductivity and hence G (Grant, Mekonnen, Riley, Wainwright, et al., 2017), contributing to small increases in ALD with $+T_a + C_a + P$ (Figure 9).

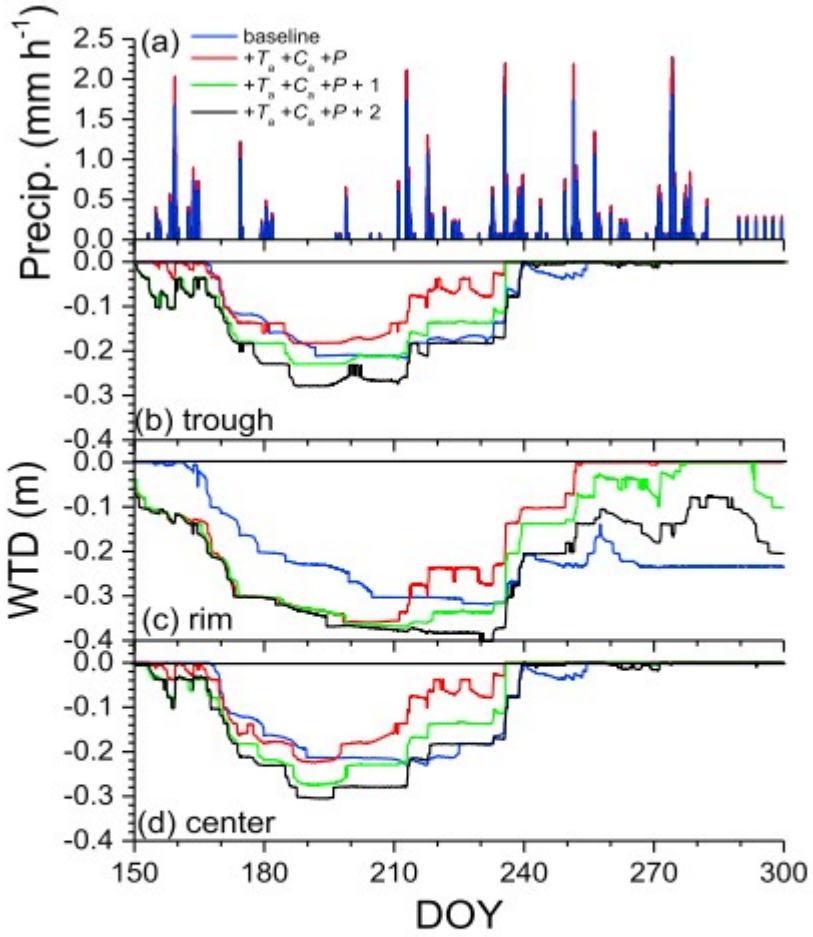

Figure 11. (a) Precipitation, and (b–d) WTD modeled during 2085 with 2015 weather in (b) troughs, (c) rims, and (d) centers of the low-centered polygon in the baseline run, in the $+T_a + C_a + P$ run and in the $+T_a + C_a + P$ run with the external water table lowered by 1 ($+T_a + C_a + P + 1$) or 2 ($+T_a + C_a + P + 2$) cm every 10 years. WTD > 0 indicates depth of surface standing water. WTD = water table depth; DOY = day of year.

Lowering the external water table by 1 or 2 cm per decade during the $+T_a + C_a + P$ runs hastened discharge and slowed recharge through the northern and southern boundaries of the modeled LCP and FCP (Figure 1). Hence, WTDs modeled in 2085 with $+T_a + C_a + P + 1$ and $+T_a + C_a + P + 2$ were greater than those with $+T_a + C_a + P$ (Figure 11). Consequent decreases in θ of surface litter and surface soil lowered thermal conductivity and hence G (Grant, Mekonnen, Riley, Wainwright, et al., 2017), so that ALD increased more slowly from increased drainage with $+T_a + C_a + P + 1$ and $+ T_a + C_a + P + 2$ than with $+T_a + C_a + P$ (Figure 12).

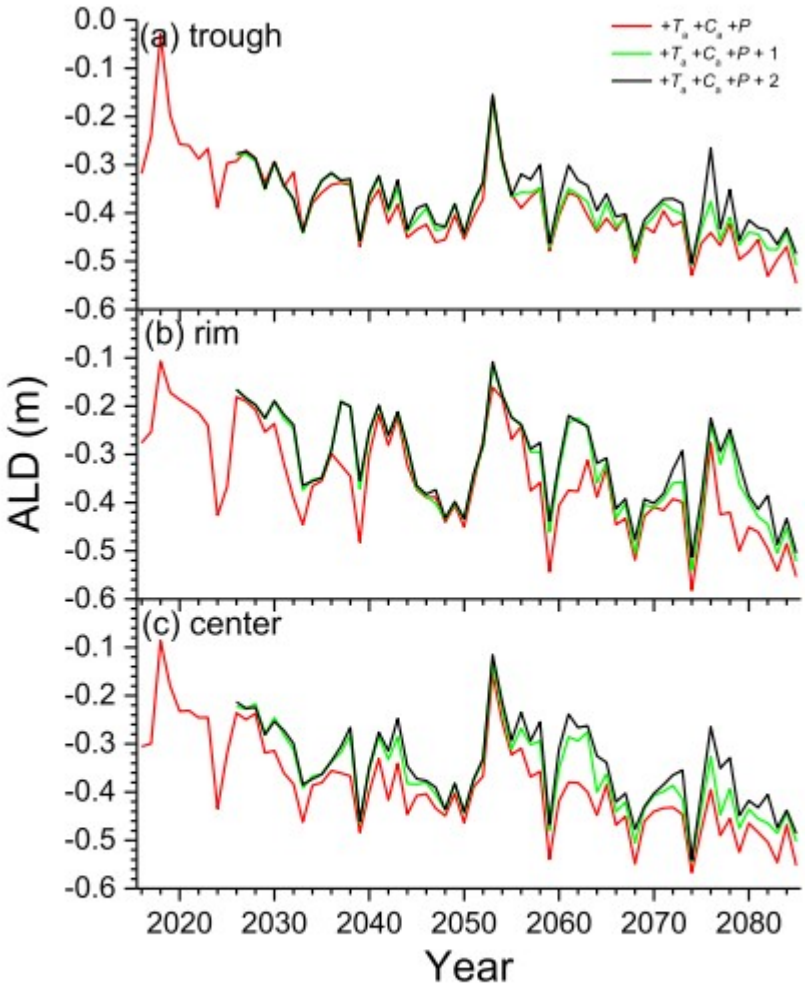

Figure 12. ALD modeled under climate change with the external water table unchanged ($+T_a + C_a + P$), or lowered by 1 ($+T_a + C_a + P + 1$) or 2 ($+T_a + C_a + P + 2$) cm every 10 years. ALD = active layer depth.

6 Discussion

6.1 Soil Water Balance and Climate Change

Shallower water tables modeled with $+T_a + C_a + P$ than in the baseline run (Figure 11) were attributed to increases in P (Table 2) that were not offset by increases in ET (Figure 7b). Modeled ET did not rise with $+T_a + C_a + P$ (Figure 7) because

1. Increased sedge LAI (Table 5) caused more R_n to be absorbed by vascular sedge and less by nonvascular moss and ground surfaces (Figure 8a). Hence, a greater fraction of LE driven by R_n [B1a] was limited by stomatal resistance (r_c) of sedge [B1c] which increased under rising C_a thereby improving water use efficiency [C5] (Grant et al., 2004). A correspondingly smaller fraction of LE was not limited by r_c, but was limited by increased overstory boundary layer resistance

(r_a) from greater sedge LAI over moss and ground surfaces. In the baseline run, the fraction of *ET* modeled from moss and ground surfaces was 70–75% of total *ET* (e.g., Figure 8b), consistent with an observation by Liljedahl et al. (2011) that 55% to 85% of *ET* in arctic coastal wetlands is evaporation from moss and open water. Any reduction in this *ET* from increased shading by overstory PFTs would likely reduce ecosystem *ET*.

The limited response of modeled *ET* to long-term $+T_a + C_a + P$ contrasted with the much greater response of modeled *ET* to short-term increases in T_s (Figure 3) and T_a (Figure 4b) during which no change in vegetation density or composition was modeled. Increases in *ET* with T_s from soil heating were driven by increases of (1) vapor pressures (e_{so}) [D6a,b], (2) gaseous diffusivity [D17], (3) boundary layer conductance with warmer ground surface [B3a], and (4) thawed soil volume [D13] which combined to increase e_{so} gradients and therefore the vapor fluxes [D6, D17]. Increases in *ET* modeled with T_a from air warming were almost entirely attributed to increases in canopy transpiration from increases in canopy vapor pressures (e_c) with T_c [B1c], and from lower canopy stomatal resistance (r_c) of the vascular PFT with more rapid CO_2 fixation [B2a]. The contrasting responses of *ET* to short-term soil heating (Figure 3) and air warming (Figure 4) and to long-term climate warming (Figure 7) indicate that the impacts on soil hydrology of long-term climate change will likely differ from those of short-term soil heating and air warming experiments.

2. Less absorption of R_n at the ground surface during growing seasons, combined with less insulation by briefer snowpacks during winters (indicated by the extended ice-free periods in Figures 5b and 5d), reduced gains in *G* (e.g., Figure 8d) and hence slowed increases of T_s relative to T_a (e.g., Figure 8e). Mean annual near-surface (2 cm) T_s (MAT_s) modeled with $+T_a + C_a + P$ increased by 2.4–3.2 °C in lower features and by 2.9–4.7 °C in higher features after 70 years, less than the increase in mean MAT_a of 6.2 °C (Table 2). The modeled increases in MAT_s relative to those in MAT_a were similar to an increase in ground surface temperature of 0.44 ± 0.05 °C per decade with an increase in MAT_a of 1.0 ± 0.8 °C per decade recorded in NW Alaska from 1996 to 2005 by Batir et al. (2017). The model results indicated that changes in T_s relative to T_a were affected by changes in densities of surface vegetation and litter, so that the relationship between increases in T_s and T_a during climate change will depend on changes in surface cover.

Smaller increases in T_s relative to T_a (Figure 8e) slowed increases in surface evaporation [D6] by reducing soil-air vapor pressure gradients from smaller increases in e_{so} relative to e_a, and also by increasing r_a from greater near-surface atmospheric stability [B3b] (Figure 8b). This modeled response of soil evaporation to long-term $+T_a + C_a + P$ contrasted with that to short-term increases in T_s from artificial soil heating when increased soil-air vapor pressure gradients and reduced r_a drove more rapid evaporation (Figure 3b).

These contrasting responses of evaporation contributed to gradual increases in θ modeled with long-term $+T_a + C_a + P$ and to decreases in θ modeled with artificial soil heating (Figure 2c). These decreases were consistent with ones of 10–20% observed in experiments with soil heating cables (e.g., Hicks Pries et al., 2017; Kamp et al., 1998; Melillo et al., 2017) and with decreases in a meta-analysis of soil warming experiments by Lu et al. (2013).

Climate change therefore caused water tables in the modeled polygonal tundra to rise (Figure 11) and soils to become wetter if the external WTD remained unchanged. This model projection contrasts with that of Lawrence et al. (2015) in which significant soil drying was simulated across the current permafrost zone under the RCP 8.5 emissions scenario. In both projections P rose more than ET, but Lawrence et al. (2015) modeled increases in drainage following permafrost thaw. However, drainage in their study was driven by an average increase in T_s of 7 °C at 1 m depth by 2100 across the current permafrost zone, which was greater than increases in MAT_s of 2.5–3.2 °C at 1 m modeled here after 70 years with $+T_a + C_a + P$ at BEO. Increased drainage was not modeled in this study if the external WTD was assumed to remain unchanged, but could be simulated by resetting the external WTD to larger values as model runs progressed (Figure 11). Such increases might represent changes in larger-scale hydrological processes that would reduce the amount of water available to maintain water tables in the costal polygonal tundra.

6.2 Active Layer Depth and Climate Change

Increases in ALD corresponding to those modeled with $+T_a + C_a + P$ (Figures 9b and 9c) have been widely observed under climate warming already in progress (Luo et al., 2016) and modeled under climate change scenarios similar to that in this study. Mekonnen, Grant, and Schwalm (2018) simulated increases in ALD of 2.3 ± 2.0 cm per decade from 1980 to 2010 across the North American Arctic using *ecosys* with the North American Regional Reanalysis meteorological data set. Determining the rate of this increase with long-term (decadal to centennial) change in climate was complicated by variability in ALD caused by short-term (interannual) changes in weather. Above-average MAT_a and P from 2009 to 2015 caused increases in modeled ALD (Figure 6) that were similar to one of *ca*. 2 cm/year measured over the same period at a moist acidic tundra site south of BEO by Mauritz et al. (2017). These increases indicated a comparatively rapid response of ALD to short-term natural warming and wetting which was readily reversed by a subsequent return to historically average weather, as more fully described in Grant, Mekonnen, Riley, Wainwright, et al. (2017).

The long-term increase in ALD modeled here was smaller than that modeled by Harp et al. (2016) who projected an increase in ALD at BEO from *ca*. 0.3 m in 2006 to nearly 0.9 m by 2100 under RCP8.5 climate change. However, carbon cycling processes driving vegetation change were not represented in their model. The increase in ALD modeled here was also smaller than that in Koven et al. (2011) who projected that ALD in the north slope region of

Alaska would increase beyond 1.2 m by 2100 with SRES A2, driven by rises in mean high-latitude surface T_s of *ca*. 8 °C.

The smaller increases in ALD modeled here were driven by increases in T_s that were smaller than those in T_a. In the baseline run, surface MAT_s was 8.0 °C higher than MAT_a, largely due to thermal insulation by snowpacks and surface litter. This increase was in the upper range of those derived by Koven et al. (2013) in a meta-analysis of the response of land surface models to high latitude warming, but was consistent with an increase derived from observations by Koven et al. (2013) of 6.2 °C. However, briefer snowpacks and greater canopy LAI caused the surface MAT_s to decline from 8.0 to 5.4 °C higher than MAT_a over 70 years of $+T_a + C_a + P$. Consequently, rises in T_s projected under climate change in this study remained lower than those projected in others (e.g., Lawrence et al., 2015), causing slower long-term increases in ALD.

The increase in spatially averaged ALD modeled with $+T_a + C_a + P$ in our study was 22.4 cm with an increase in MAT_a of 6.16 °C after 70 years, giving a ΔALD:ΔMAT_a ratio of 3.6 cm per degree Celsius. This ratio was among the lowest of those from the land surface models included in the meta-analysis by Koven et al. (2013) of the response of land surface models to high latitude warming. However, Koven et al. concluded that ΔALD:ΔMAT_a ratios in most of these models were greater that those derived from observations of 3 cm per degree Celsius, close to that modeled here. The ΔALD:ΔMAT_a ratios modeled with $+T_a + C_a + P$ in this study were even lower if soil wetting and its effects on ALD (Grant, Mekonnen, Riley, Arora, et al., 2017) were reduced by excluding increases in P (Figure 10), or by altering boundary conditions to increase drainage with $+T_a + C_a + P + 1$ or +2 (Figure 12).

The smaller increase in ALD with climate change modeled in this study compared to those in previous studies was attributed in part to increasing sedge and moss LAI (Table 5) which reduced soil R_n, G, and hence soil warming (Figure 8). The increases in LAI of sedge relative to moss modeled in this study were consistent with findings by Elmendorf et al. (2012) and M. D. Walker et al. (2006) from meta-analyses of observations from artificial warming experiments across the arctic in which warming increased height and cover of deciduous shrubs and graminoids and decreased cover of mosses and lichens. The effects of greater vegetation cover on slowing increases of ALD modeled with $+T_a + C_a + P$ in this study were consistent with observations from a meta-analysis by D. A. Walker et al. (2003) that taller, denser plant canopies and thicker organic horizons in warmer climates counter the effects of increased T_a on ALD.

The smaller increase in ALD modeled here may also be attributed to detailed representations of heat transfer processes through snowpacks, and through surface litter and organic surface layers with low bulk densities and large ice-filled porosities (e.g., Figure 5), indicated by Schaefer et al. (2014) as processes needing improved representation in models used to project

permafrost degradation with climate change. These heat transfer processes constrained modeled G to values consistent with measurements (e.g., Figure 4b) indicating realistic rates of soil warming and cooling under specified changes in surface boundary conditions. Projections of climate change impacts on Arctic hydrology must therefore account for effects on heat transfers of vegetative growth and ground surface characteristics.

The effects of vegetative growth on ALD modeled here were influenced by the low stature of the nonwoody PFTs included in the simulation. These effects may have been different had taller woody PFTs been included that protruded through the snowpack, thereby altering albedo. In a fully coupled model run, Lawrence and Swenson (2011) simulated increases in ALD of *ca*. 10 cm with a 20% increase in shrub cover from increased T_a caused by reduced winter albedo. In *ecosys* runs including woody shrubs (e.g., Mekonnen, Riley, & Grant, 2018), most of the increase in ecosystem R_n modeled with reduced winter albedo is dissipated as H which, in a fully coupled run could raise T_a and hence increase heat advection that could increase ALD slightly from that modeled here. However, these increases would be offset by reduced R_n modeled at snow and soil surfaces from increased shading by shrubs.

A methodology for linking *ecosys* to large-scale databases of weather, soils, PFTs, and land uses has been developed with early results appearing in Mekonnen, Grant, and Schwalm (2018) and Mekonnen, Riley, and Grant (2018). A key advance in this methodology will be the incorporation of representative topographic characteristics such as polygons into these databases, enabling the large-scale modeling of topographic effects on ALD and ecosystem productivity.

7 Summary

1. RCP 8.5 climate change from 2015 to 2085 altered energy exchange by increasing LAI of dominant sedge relative to that of moss.
2. Increased C_a and sedge LAI imposed greater stomatal control of transpiration and reduced soil heat fluxes, slowing soil warming, limiting increases in ET, and thereby causing gradual soil wetting.
3. Consequently, increases in soil surface temperatures of 2.4–4.7 °C and active layer depths of 21–24 cm above current values were modeled after 70 years. These increases varied with elevation within the polygonal landscape.
4. ALD increase was slowed if model boundary conditions were altered to improve landscape drainage.
5. Accounting for climate change effects on vegetation density and composition, and consequent effects on surface energy budgets, will cause slower increases in soil temperatures and active layer depths to be modeled during climate change simulations.

Acknowledgments

High performance computing facilities for *ecosys* were provided by Compute Canada (www.computecanada.ca) through the WestGrid computing network (https://www.westgrid.ca). Field research was supported by the Director, Office of Science, Office of Biological and Environmental Research of the U.S. Department of Energy under contract DE-AC02-05CH11231 to Lawrence Berkeley National Laboratory as part of the Next-Generation Ecosystem Experiments in the Arctic (NGEE-Arctic) project. Data used in this paper are available from the NGEE website as cited in the text.

References

Avis, C. A., Weaver, A. J., & Meissner, K. J. (2011). Reduction in areal extent of high-latitude wetlands in response to permafrost thaw. *Nature Geoscience*, 4, 444– 448. https://doi.org/10.1038/ngeo1160

Batir, J. F., Hornbach, M. J., & Blackwell, D. D. (2017). Ten years of measurements and modeling of soil temperature changes and their effects on permafrost in northwestern Alaska. *Global and Planetary Change*, 148, 55– 71. https://doi.org/10.1016/j.gloplacha.2016.11.009

Billesbach, D. P. (2011). Estimating uncertainties in individual eddy covariance flux measurements: A comparison of methods and a proposed new method. *Agricultural and Forest Meteorology*, 151, 394– 405. https://doi.org/10.1016/j.agrformet.2010.12.001

Bintanja, R., & Selten, F. M. (2014). Future increases in Arctic precipitation linked to local evaporation and sea-ice retreat. *Nature*, 509(7501), 479– 482. https://doi.org/10.1038/nature13259

Dafflon, B., Hubbard, S., Ulrich, C., Peterson, J., Wu, Y., Wainwright, H., & Kneafsey, T. J. (2016). Geophysical estimation of shallow permafrost distribution and properties in an ice-wedge polygon-dominated Arctic tundra region. *Geophysics*, 81, WA247– WA263. https://doi.org/10.1190/geo2015-0175.1

Dafflon, B., Oktem, R., Peterson, J., Ulrich, C., Tran, A. P., Romanovsky, V., & Hubbard, S. S. (2017). Coincident aboveground and belowground autonomous monitoring to quantify covariability in permafrost, soil, and vegetation properties in Arctic tundra. *Journal of Geophysical Research: Biogeosciences*, 122, 1321– 1342. https://doi.org/10.1002/2016JG003724

Dengel, S., Torn, M. S., & Billesbach, D. (2017). Eddy-Covariance and auxiliary measurements, NGEE-Barrow, 2012–2016. Retrieved from http://ngee-arctic.ornl.gov/, accessed 21.11.2017.

Elmendorf, S. C., Henry, G. H. R., Hollister, R. D., Björk, R. G., Boulanger-Lapointe, N., Cooper, E. J., Cornelissen, J. H. C., Day, T. A., Dorrepaal, E., Elumeeva, T. G., Gill, M., Gould, W. A., Harte, J., Hik, D. S., Hofgaard, A., Johnson, D. R., Johnstone, J. F., Jónsdóttir, I. S., Jorgenson, J. C., Klanderud, K., Klein, J. A., Koh, S., Kudo, G., Lara, M., Lévesque, E., Magnússon, B., May, J.

L., Mercado-Dı´az, J. A., Michelsen, A., Molau, U., Myers-Smith, I. H., Oberbauer, S. F., Onipchenko, V. G., Rixen, C., Martin Schmidt, N., Shaver, G. R., Spasojevic, M. J., Þórhallsdóttir, Þ. E., Tolvanen, A., Troxler, T., Tweedie, C. E., Villareal, S., Wahren, C. H., Walker, X., Webber, P. J., Welker, J. M., & Wipf, S. (2012). Plot-scale evidence of tundra vegetation change and links to recent summer warming. *Nature Climate Change*, 2, 453– 457. https://doi.org/10.1038/nclimate1465

Gentine, P., Entekhabi, D., & Heusinkveld, B. (2012). Systematic errors in ground heat flux estimation and their correction. *Water Resources Research*, 48, W09541. https://doi.org/10.1029/2010WR010203

Grant, R. F. (2015). Ecosystem CO_2 and CH_4 exchange in a mixed tundra and a fen within a hydrologically diverse Arctic landscape. Part II. Modelled impacts of climate change. *Journal of Geophysical Research: Biogeosciences*, 120, 1388– 1406. https://doi.org/10.1002/2014JG002889

Grant, R. F., Kimball, B. A., Wall, G. W., Triggs, J. M., Brooks, T. J., Pinter, P. Jr., Conley, M. M., Ottman, M. J., Lamorte, R. L., Leavitt, S. W., Thompson, T. L., & Matthias, A. D. (2004). How elevated CO_2 affects water relations, water use and growth of irrigated sorghum: Testing a model with results from a Free Air CO_2 Enrichment (FACE) experiment. *Agronomy Journal*, 96, 1693– 1705. https://doi.org/10.2134/agronj2004.1693

Grant, R. F., Mekonnen, Z. A., Riley, W. J., Arora, B., & Torn, M. S. (2017). Mathematical modelling of arctic polygonal tundra with *ecosys*: 2. Microtopography determines how CO_2 and CH_4 exchange responds to changes in temperature and precipitation. *Journal of Geophysical Research: Biogeosciences*, 122, 3174– 3187. https://doi.org/10.1002/2017JG004037

Grant, R. F., Mekonnen, Z. A., Riley, W. J., Arora, B., & Torn, M. S. (2019). Modelling climate change impacts on an Arctic polygonal tundra. Part 2: Changes in CO2 and CH4 exchange depend on rates of permafrost thaw as affected by changes in vegetation and drainage. *Journal of Geophysical Research: Biogeosciences*, 124. https://doi.org/10.1029/2018JG004645

Grant, R. F., Mekonnen, Z. A., Riley, W. J., Wainwright, H. M., Graham, D., & Torn, M. S. (2017). Mathematical modelling of arctic polygonal tundra with *ecosys*: 1. Microtopography determines how active layer depths respond to changes in temperature and precipitation. *Journal of Geophysical Research: Biogeosciences*, 122, 3161– 3173. https://doi.org/10.1002/2017JG004035

Harp, D. R., Atchley, A. L., Painter, S. L., Coon, E. T., Wilson, C. J., Romanovsky, V. E., & Rowland, J. C. (2016). Effect of soil property uncertainties on permafrost thaw projections: A calibration-constrained analysis. *The Cryosphere*, 10, 341– 358. https://doi.org/10.5194/tc-10-341-2016

Hicks Pries, C. E., Castanha, C., Porras, R. C., & Torn, M. S. (2017). The whole-soil carbon flux in response to warming. *Science*, 355(6332), 1420– 1423. 28280251. https://doi.org/10.1126/science.aal1319

Hinzman, L., Romanovsky, V., Cable, W., & Busey, G. (2016). Surface meteorology, Barrow, Alaska, Area A, B, C and D, ongoing from 2012. Retrieved from http://ngee-arctic.ornl.gov/, accessed 19 January 2016.

Kamp, T., Steindl, H., Hantschel, R. E., Beese, F., & Munch, J.-C. (1998). Nitrous oxide emissions from a fallow and wheat field as affected by increased soil temperatures. *Biology and Fertility of Soils*, 27, 307– 314. https://doi.org/10.1007/s003740050438

Koven, C. D., Riley, W. J., & Stern, A. (2013). Analysis of permafrost thermal dynamics and response to climate change in the CMIP5 Earth system models. *Journal of Climate*, 26, 1877– 1900. https://doi.org/10.1175/JCLI-D-12-00228.1

Koven, C. D., Ringeval, B., Friedlingstein, P., Ciais, P., Cadule, P., Khvorostyanov, D., Krinner, G., & Tarnocai, C. (2011). Permafrost carbon-climate feedbacks accelerate global warming. *Proceedings of the National Academy of Sciences*, 108(36), 14,769– 14,774. https://doi.org/10.1073/pnas.1103910108

Kumar, J., Collier, N., Bisht, G., Mills, R. T., Thornton, P. E., Iversen, C. M., & Romanovsky, V. (2016). Modeling the spatiotemporal variability in subsurface thermal regimes across a low-relief polygonal tundra landscape. *The Cryosphere*, 10, 2241– 2274. https://doi.org/10.5194/tc-10-2241-2016

Lawrence, D. M., Koven, C. D., Swenson, S. C., Riley, W. J., & Slater, A. G. (2015). Permafrost thaw and resulting soil moisture changes regulate projected high-latitude CO_2 and CH_4 emissions. *Environmental Research Letters*, 10, 094011. https://doi.org/10.1088/1748-9326/10/9/094011

Lawrence, D. M., & Swenson, S. C. (2011). Permafrost response to increasing Arctic shrub abundance depends on the relative influence of shrubs on local soil cooling versus large-scale climate warming. *Environmental Research Letters*, 6, 045504. https://doi.org/10.1088/1748-9326/6/4/045504

Leffler, A. J., Klein, E. S., Oberbauer, S. F., & Welker, J. M. (2016). Coupled long-term summer warming and deeper snow alters species composition and stimulates gross primary productivity in tussock tundra. *Oecologia*, 181, 287– 297. https://doi.org/10.1007/s00442-015-3543-8

Liljedahl, A. K., Hinzman, L. D., Harazono, Y., Zona, D., Tweedie, C. E., Hollister, R. D., Engstrom, R., & Oechel, W. C. (2011). Nonlinear controls on evapotranspiration in arctic coastal wetlands. *Biogeosciences*, 8, 3375– 3389. https://doi.org/10.5194/bg-8-3375-2011

Liljedahl, A. K., Hinzman, L. D., & Schulla, J. (2012). Ice-wedge polygon type controls low-gradient watershed-scale hydrology. In K. M. Hinkel (Ed.), *Tenth*

International Conference on Permafrost, International Contributions (Vol. 1, pp. 231– 236). Salekhard, Russia: The Northern Publisher.

Lu, M., Zhou, X., Yang, Q., Li, H., Luo, Y., Fang, C., Chen, J., Yang, X., & Li, B. (2013). Responses of ecosystem carbon cycle to experimental warming: A meta-analysis. *Ecology*, 94(3), 726– 738. https://doi.org/10.1890/12-0279.1

Luo, D., Wu, Q., Jin, H., Marchenko, S. S., Lu, L., & Gao, S. (2016). Recent changes in the active layer thickness across the northern hemisphere. *Environment and Earth Science*, 75, 555. https://doi.org/10.1007/s12665-015-5229-2

Mauritz, M., Bracho, R., Celis, G., Hutchings, J., Natali, S. M., Pegoraro, E., Salmon, V. G., Schädel, C., Webb, E. E., & Schuur, E. A. G. (2017). Nonlinear CO_2 flux response to 7 years of experimentally induced permafrost thaw. *Global Change Biology*, 23, 3646– 3666. https://doi.org/10.1111/gcb.13661

Mekonnen, Z. A., Grant, R. F., & Schwalm, C. (2018). Modelling impacts of recent warming on seasonal carbon exchange in higher latitudes of North America. *Arctic Science*, 4(4), 471– 484. https://doi.org/10.1139/as-2016-0009

Mekonnen, Z. A., Riley, W. J., & Grant, R. F. (2018). Accelerated nutrient cycling and increased light competition will lead to 21st century shrub expansion in North American Arctic tundra. *Journal of Geophysical Research: Biogeosciences*, 123, 1683– 1701. https://doi.org/10.1029/2017JG004319

Melillo, J., Steudler, P., & Mohan, J. (2017). Barre woods soil warming experiment at Harvard Forest since 2001. Harvard Forest Data Archive: HF018.

Peterson, J. (2017). Active layer and moisture measurements for intensive site 0 and 1, Barrow, Alaska. Retrieved from http://ngee-arctic.ornl.gov/, accessed 2.11.2017.

Romanovsky, V., & Cable, W. (2017). Subsurface temperature, moisture, thermal conductivity and heat flux, Barrow, Area A, B, C, D. Retrieved from http://ngee-arctic.ornl.gov/, accessed 2.11.2017.

Schaefer, K., Lantuit, H., Romanovsky, V. E., Schuur, E. A. G., & Witt, R. (2014). The impact of the permafrost carbon feedback on global climate. *Environmental Research Letters*, 9, 085003. https://doi.org/10.1088/1748-9326/9/8/085003

Schuur, E. A. G., McGuire, A. D., Schädel, C., Grosse, G., Harden, J. W., Hayes, D. J., Hugelius, G., Koven, C. D., Kuhry, P., Lawrence, D. M., Natali, S. M., Olefeldt, D., Romanovsky, V. E., Schaefer, K., Turetsky, M. R., Treat, C. C., & Vonk, J. E. (2015). Climate change and the permafrost carbon feedback. *Nature*, 520, 171– 179. https://doi.org/10.1038/nature14338

Sclater, J. G., Jaupart, C., & Galson, D. (1980). The heat flow through oceanic and continental crust and the heat loss of the Earth. *Reviews of Geophysics and Space Physics*, 18, 269– 311. https://doi.org/10.1029/RG018i001p00269

Shiklomanov, N. I., Streletskiy, D. A., Nelson, F. E., Hollister, R. D., Romanovsky, V. E., Tweedie, C. E., Bockheim, J. G., & Brown, J. (2010). Decadal variations of active-layer thickness in moisture-controlled landscapes, Barrow, Alaska. *Journal of Geophysical Research*, 115, G00I04. https://doi.org/10.1029/2009JG001248

Vaughn, L. J. S., Conrad, M. E., Bill, M., & Torn, M. S. (2016). Isotopic insights into methane production, oxidation, and emissions in Arctic polygon tundra. *Global Change Biology*, 22(10), 3487– 3502. https://doi.org/10.1111/gcb.13281

Wainwright, H. M., Dafflon, B., Smith, L. J., Hahn, M. S., Curtis, J. B., Wu, Y., Ulrich, C., Peterson, J. E., Torn, M. S., & Hubbard, S. S. (2015). Identifying multiscale zonation and assessing the relative importance of polygon geomorphology on carbon fluxes in an Arctic tundra ecosystem. *Journal of Geophysical Research: Biogeosciences*, 120, 788– 808. https://doi.org/10.1002/2014JG002799

Walker, D. A., Jia, G. J., Epstein, H. E., Raynolds, M. K., ChapinIII, F. S., Copass, C., Hinzman, L. D., Knudson, J. A., Maier, H. A., Michaelson, G. J., Nelson, F., Ping, C. L., Romanovsky, V. E., & Shiklomanov, N. (2003). Vegetation-soil-thaw-depth relationships along a low-Arctic bioclimate gradient, Alaska: Synthesis of information from the ATLAS studies. *Permafrost and Periglacial Processes*, 14, 103– 123. https://doi.org/10.1002/ppp.452

Walker, M. D., Wahren, C. H., Hollister, R. D., Henry, G. H. R., Ahlquist, L. E., Alatalo, J. M., Bret-Harte, M. S., Calef, M. P., Callaghan, T. V., Carroll, A. B., Epstein, H. E., Jonsdottir, I. S., Klein, J. A., Magnusson, B., Molau, U., Oberbauer, S. F., Rewa, S. P., Robinson, C. H., Shaver, G. R., Suding, K. N., Thompson, C. C., Tolvanen, A., Totland, O., Turner, P. L., Tweedie, C. E., Webber, P. J., & Wookey, P. A. (2006). Plant community responses to experimental warming across the tundra biome). *PNAS*, 103, 1342– 1346. https://doi.org/10.1073/pnas.0503198103

Wentworth, G. R., Murphy, J. G., Croft, B., Martin, R. V., Pierce, J. R., Côté, J.-S., Courchesne, I., Tremblay, J. É., Gagnon, J., Thomas, J. L., Sharma, S., Toom-Sauntry, D., Chivulescu, A., Levasseur, M., & Abbatt, J. P. D. (2016). Ammonia in the summertime Arctic marine boundary layer: Sources, sinks, and implications. *Atmospheric Chemistry and Physics*, 16(4), 1937– 1953. https://doi.org/10.5194/acp-16-1937-2016

Woo, M. K., & Guan, X. J. (2006). Hydrological connectivity and seasonal storage change of tundra ponds in a polar oasis environment. *Permafrost and Periglacial Processes*, 17, 309– 323. https://doi.org/10.1002/ppp.565

Wood, S., Curtis, J. B., Norby, R., Liebig, J., Iversen, C., Sloan, V., Rogers, A., Brooks, B. & Hahn, M. (2015). Soil temperature, soil moisture and thaw depth, Barrow, Alaska, Ver.1. Retrieved from http://ngee-arctic.ornl.gov/, accessed 19.11.2015.

Xu, X., & Yuan, F. (2016). Meteorological forcing at Barrow AK 1981–2013. Retrieved from http://ngee-arctic.ornl.gov/, accessed 22 June 2016.

Zona, D., Lipson, D. A., Zulueta, R. C., Oberbauer, S. F., & Oechel, W. C. (2011). Microtopographic controls on ecosystem functioning in the Arctic coastal plain. *Journal of Geophysical Research*, 116, G00I08. https://doi.org/10.1029/2009JG001